# Assessment of the interplay between scaffold geometry, induced shear stresses and cell proliferation within a packed bed perfusion bioreactor

Roman Thibeaux, Herve Duval, Benjamin Smaniotto, Elsa Vennat, David Néron, Bertrand David

**Title**

Assessment of the interplay between scaffold geometry, induced shear stresses and cell proliferation within a packed bed perfusion bioreactor.

**Running tittle**

Assessment of optimal shear stress within a bioreactor

Roman Thibeaux[1†$], Ph.D., Hervé Duval[3$], Ph.D., Benjamin Smaniotto[2], Elsa Vennat[1], Ph.D., David Néron[2], Ph.D., and Bertrand David[1], Ph.D.

(1) MSSMat, CentraleSupélec, Université Paris Saclay, CNRS, F-91190 Gif sur Yvette, France

(2) LMT, ENS Paris-Saclay, CNRS, Université Paris-Saclay, F-94235 Cachan, France

(3) LGPM, CentraleSupélec, Université Paris Saclay, F-91190 Gif sur Yvette, France

(†) Current affiliation: Institut Pasteur in New Caledonia, Institut Pasteur International Network, Leptospirosis Research and Expertise Unit, Noumea, New Caledonia

($) Roman Thibeaux and Hervé Duval have contributed equally to this work

**Corresponding author:**

Bertrand David, Ph.D.

CentraleSupélec

UMR CNRS 8579

Laboratoire de Mécanique des Sols, Structures et Matériaux

3 rue Joliot-Curie

F-91 190 Gif sur Yvette

Telephone: 33 (0)1.75.31.61.53

26 E-mail: bertrand.david@centralesupelec.fr

## Abstract

By favouring cell proliferation and differentiation, perfusion bioreactors proved efficient at optimizing cell culture. The aim of this study was to quantify cell proliferation within a perfusion bioreactor and correlate it to the wall shear stress distribution by combining 3-D imaging and computational fluid dynamics simulations.

NIH-3T3 fibroblasts were cultured onto a scaffold model made of impermeable polyacetal spheres or Polydimethylsiloxane cubes. After 1, 2 and 3 weeks of culture, constructs were analysed by micro-computed tomography (μCT) and quantification of cell proliferation was assessed. After 3 weeks, the volume of cells was found four times higher in the stacking of spheres than in the stacking of cube.

3D-μCT reconstruction of bioreactors was used as input for the numerical simulations. Using a lattice-Boltzmann method, we simulated the fluid flow within the bioreactors. We retrieved the wall shear stress (WSS) distribution (PDF) on the scaffolds surface at the beginning of cultivation and correlated this distribution to the local presence of cells after three weeks of cultivation. We found that the WSS distributions strongly differ between spheres and cubes even if the porosity and the specific wetted area of the stackings were very similar. The PDF is narrower and the mean WSS is lower for cubes (11 mPa) than for spheres (20 mPa). For the stacking of spheres, the relative occupancy of the surface sites by cells is maximal when WSS is greater than 20 mPa. For cubes, the relative occupancy is maximal when the WSS is lower than 10 mPa. The discrepancies between spheres and cubes are attributed to the more numerous sites in stacking of spheres that may induce 3-D (multi-layered) proliferation.

# Introduction

Perfusion bioreactors are widely used in musculoskeletal tissue engineering [1–5]. Bone cells are sensitive to wall shear stress (WSS) [6–15], influencing cell fate through mechanotransduction [16–20], resulting in an enhancement of cell proliferation and/or differentiation [1,6,7,21–24]. The capacity of a perfusion bioreactor to lead to bone tissue has been demonstrated using animal models [2,25]. Two strategies can be implemented to investigate WSS influence at the single-cell scale. The first involves developing dedicated microsystems to study the phenomena and then transferring the results to the bioreactor scale. The second requires examining the bioreactor scale directly and using the appropriate means to collect information at the single-cell scale. The heterogeneity of the local conditions encountered within a bioreactor limits *a priori* the interpretation of the results. However, if the heterogeneity of local conditions is known (using numerical simulation), this understanding grants access to an information bank that, can then be statistically analysed.

Today, histology is still the standard method for investigating engineered constructs. However, this method provides only a partial visualization of the construct. Many researches have attempted to use micro-computed tomography (μCT) to determine porosity or other characteristics within the scaffold as an alternative to histology. This technique allows for visualization and quantification of dense structures, and includes the possibility of investigating the influence of scaffold features, such as the internal pore architecture with regard to the growth of cells within the scaffold [26–30]. Authors have previously reported that μCT can be used to image and segment microporous scaffolds seeded with mesenchymal stem cells (MSCs) and cultured to produce soft tissue and mineralized tissue in a bioreactor with a high degree of accurancy [28,30]. Furthermore, image processing is a key factor in establishing a relevant method for separating different phases (porosity, cells and biomaterials) from μCT images [31]. Authors managed to segment images using an in-house segmentation algorithm

[28,29]. 3D-μCT reconstructions can be used to simulate flow and model the relationship between cell proliferation and mechanical quantities, including shear stress. Thus, these reconstructions help determine which solicitations that seem to be the most favourable for cell expansion. Authors report a proof-of-principle, demonstrating that it is possible to model the real geometrical and hydro-dynamical microenvironment within a scaffold and the presence of cells in micro-pores. Various modelling approaches carried out within the last decade are reported in the literature [32–35]. To evaluate the localized fluid shear stress distributions throughout the culture period from micro-tomography images, giving an indication of the effects of tissue growth on the flow-induced stress field, the authors deployed fluid dynamic simulations using a custom in-house lattice Boltzmann (LBM) program [30]. LBM easily handles complex geometries such as porous media. After binarization, the 3D-μCT image of a porous medium can be used directly by the LBM code (just by locating the nodes of the lattice at the centre of the voxels).

This paper describes a method to identify the WSS optimal range for cell proliferation within constructs cultured in a packed bed bioreactor. This method is based on a combined analysis of micro-tomography images and Computational fluid dynamics (CFD) simulations. We present an illustration based on a bioreactor having demonstrated its ability to produce bone constructs resulting in bone formation in a large animal [2]. Because our aim was not to produce a bone construct, but rather to establish and validate a method, we chose to use fibroblast cells because of their known mechanosensitivity [36], cultured onto biocompatible [37] impermeable Polyacetal (POM) spheres or Polydimethylsiloxane (PDMS) cubes within the bioreactor. POM spheres have several excellent qualities, including wear resistance, low moisture absorption, dimensional stability, good fatigue strength and thermal stability [38–40]. After 1, 2 or 3 weeks of culture, samples were analysed using a 3D imaging system based on μCT. We made the cells dense to X-rays using osmium-tetroxide staining. By combining this imaging

100 method with image processing and analysis, we quantified the cell proliferation according
101 time. We used the μCT 3D reconstruction of our bioreactors as input for the CFD simulations.
102 Fluid flow was simulated within the packed bed perfusion bioreactors using a LBM. We
103 analysed the wall shear stress distribution provided by the numerical simulation together with
104 the scaffold surface coverage with cells to identify the wall shear stress values that were most
105 favourable to proliferation.

106

# Materials and methods

## Cell line

Murine fibroblasts NIH/3T3 (ATCC) were cultured in DMEM Glutamax (Gibco) supplemented with 10% Foetal Calf Serum (Pan-Biotech) in standard conditions (37 °C, 5% CO2, 100% humidity).

## Perfusion bioreactor system

A pre-approved, custom-made perfusion bioreactor [2] was used in the present study. The perfusion bioreactor was connected to a reservoir containing the culture medium in a closed loop arrangement of platinum-cured silicone tubing (Masterflex). The perfusion bioreactor was located within an incubator set at 37℃. The peristaltic pump (Masterflex) was set up to deliver a flow rate $Q$ of 10 mL/min. This design allowed the medium to flow from the reservoir to an entry chamber located at the bottom of the perfusion bioreactor, preventing fluid flow disturbances and maintaining uniform flow conditions. To maintain sample integrity when extracting the sample from the bioreactor, we placed inside the perfusion chamber a Polypropylene tube (inner diameter 12 mm, 50 mm height) that was designed to fit the chamber's internal diameter. This ensured that the media would flow within the tube. A grid (with pores of 1 mm in diameter) separated the entry from the perfusion bioreactor chamber (where scaffolds were placed during experiments).

## 3D spheres or cubes-based constructs

We used nonporous biocompatible 3D materials in our experiments. Polyacetal spheres (2mm Ø) (Marteau & Lemarié) or Polydimethylsiloxane cubes (3mm*3mm*3mm) (Sylgard®, custom-made mold) acted as a scaffold (packed bed configuration). Materials 'dimension

were chosen according to previous study [2] to comply with a rough porosity of 50% and an estimated shear stress up to 100mPa.

**Seeding and culturing cells in perfusion bioreactor**

Tubes (15mL) were filled with 300 POM spheres or 60 PDMS cubes. Prior to cell seeding, scaffolds were treated with fibronectin (10 mg/mL, 1 hour, 37°c, Roche). 75% confluent 3T3 cells ($10^6$ cells/mL) were then seeded onto the scaffold. Scaffolds were let overnight in a 5% $CO_2$ incubator. To assess cell number, control samples (n=2) were performed. Cell number was assessed after trypsinization (1 x 10 min) using Malassez cell.

After 24 hours, seeded scaffolds were placed within the perfusion bioreactor and the medium was allowed to flow at a continuous rate of $Q = 10$ mL/min. Once a week the medium (200mL) was renewed. Culture under perfusion was carried out for 1, 2 and 3 weeks. For each time point, the results reported are average values of 3 independent experiments.

**Sample preparation for X-ray micro-tomography.**

At the indicated time points, constructs were fixed overnight (4% PFA in PBS, Sigma-Aldrich), washed with PBS and stained overnight with 1% osmium-tetroxide ($OsO_4$ in PBS, Alpha Aesar) to increase cellular contrast and makes them visible by µCT. After staining, samples were dehydrated by gradually increasing ethanol bath at 25, 50, 70, 90, 95, and 100%. A final bath of hexamethyldisilazane (Sigma) was performed to completely dry out the sample. HMDS drying is a good alternative to critical point drying in the preparation of the samples. This method is time and cost-effective [41], as well as optimal in order to dehydrate cells (low distortion) [42].

**X-ray computed micro-tomography image acquisition**

A μCT system X-view X 50-CT (North Star Imaging), was used to non-destructively image and quantify biomass production for each sample. μCT experiments were performed with a target of Molybdenum producing a polychromatic beam used for low absorption samples. Acquisition setup was the following: the accelerating voltage was set to 50 kV with a tube current of 400 μA. 1,200 projections were obtained from each sample over 360° (0.3° intervals) with an exposure time of 3 seconds per projection (averaging of 20 images). The transmitted beam was detected by a CMOS image sensor (3888*3072 pixels) coupled to a CsI scintillator. Each sample was scanned with a pixel size of 17 μm*17 μm, yielding a field of view of about 3 cm. The average scanning time of each specimen was 90 minutes.

**Image reconstruction, visualization and analysis**

efX-ct software (North Star Imaging) was used to reconstruct the 2D absorption projection images, generating a set of cross-sectional slices of the scaffold. Greyscale images were then exported as 16 bit images for quantitative purposes. We used ImageJ software 1.48V to process and quantify X-CT images. The region of interest corresponded to the volume delimited by the inner wall of the bioreactor. For each bioreactor, we measured the construct porosity and the volume of the cellular phase.16 bits RAW images were segmented using a thresholding method to separate scaffolds from the cells. Threshold values were retrieved from the mean of all samples (either POM spheres or PDMS cubes). Additional image processing was performed. First, a linear calibration and a Gaussian Blur mask were performed on the constructs and background respectively to homogenize the grey scale value. Then, a region of interest was determined, corresponding to the volume delimited by the inner wall of the bioreactor. Finally, cells and constructs were extracted from images using ImageJParticleAnalyzer3D plugin.

**Fluid Flow Simulations**

175 Following Porter [43], we computed the fluid flow within the perfusion bioreactor and the shear
176 stress distribution at the solid-fluid interface using an in-house lattice-Boltzmann code.
177 Lattice-Boltzmann methods are particularly well-suited to investigate fluid flow at low
178 Reynolds number in complex geometries.

179 The culture medium is assumed to be incompressible and Newtonian. Its dynamic viscosity at
180 37°C is estimated at $\mu = 10^{-3}$ Pa.s [44]. The natural convection within the bioreactor is
181 neglected compared to the forced convection due to the perfusion since the Richardson
182 number (estimated with the temperature accuracy of the incubator, *i.e.* about 0.1°C, and the
183 materials size) is significantly lower than 1 ($\mathrm{Ri} \approx 0.1$). The flow can therefore be considered
184 as isothermal. The particle Reynolds number (estimated with the bead or cube size) is equal to
185 $\mathrm{Re} \approx 3 - 4.5$. According to Bağcı[45], the perfusion flow within the granular bed formed by the
186 POM beads or the PDMS cubes is thus in the Darcy regime ($\mathrm{Re} \leq 22$).

187 The fluid flow within the bioreactor can be described by the well-known continuity and
188 Navier-Stokes equations. We simulated these equations using the multiple-relaxation-time
189 lattice-Boltzmann Method (MRT LBM) proposed by d'Humières [46] with a cubic lattice in 3
190 dimensions and 19 velocities, *i.e.* $d3q19$ (see Supplementary material, Fig. S1). We remind
191 that a LBM is built as follows: first of all, the d-dimensional space is mapped on a regular
192 lattice. Two types of lattice nodes are distinguished: the first type corresponds to the solid
193 phase, the second to the space left to the fluid. A population of fictitious particles is allocated
194 to each node of the space filled by the fluid. The velocity distribution of the population is
195 discrete. $q$ particle velocity vectors are defined: one velocity vector is the null vector and the
196 others are associated with the links between a node and its $(q-1)$ neighbors. At each time
197 increment, the population dynamics is divided into two steps: propagation of the fictitious
198 particles from node to node according to their velocity, then relaxation of the particle

populations toward equilibrium. LBM is formulated to recover the Navier–Stokes equations as the macroscopic behavior of the fictitious particles.

The evolution equation of the particle population $f_i$ with velocity $\vec{c}_i$ located at the position $\vec{r}$ at time $t$ typically reads (in lattice units):

$$f_i(\vec{r} + \vec{c}_i, t+1) = f_i(\vec{r}, t) + \mathcal{C}_i\left(\left(f_j(\vec{r}, t)\right)_{j=0,q}\right) \quad (1)$$

where $\mathcal{C}_i$ is the collision operator. We used a collision operator with two relaxation parameters [47]. The first one, $\omega_1$, depends on the fluid kinematic viscosity $\nu$:

$$\nu = c_s^2\left(\frac{1}{\omega_1} - \frac{1}{2}\right)\frac{\Delta x^2}{\Delta t} \quad (2)$$

with $c_s$ the intrinsic speed of sound of the LBM ($c_s^2 = 1/3$ in lattice units), $\Delta x$ the lattice spacing (in real units) and $\Delta t$ the time step (in real units). The second one, $\omega_2$, is fixed through the so-called "magic number combination" in order to minimize the spatial error associated with the bounce-back wall location [48]:

$$\omega_2 = 8\frac{2 - \omega_1}{8 - \omega_1} \quad (3)$$

The hydrodynamic quantities we are interested in, are the moments of the velocity distribution $(f_i)_{i=0,q}$. The fluid pressure $P$ (in real units) is related to the zeroth order velocity moment:

$$P = \rho\left(\frac{\Delta x}{\Delta t}\right)^2 c_s^2 \sum_{i=0}^{q} f_i \quad (4)$$

with $\rho$ the fluid density (in real units). The fluid velocity $\vec{v}$ (in real units) is the first order velocity moment:

$$\vec{v} = \frac{\Delta x}{\Delta t} \sum_{i=0}^{q} f_i \, \vec{c}_i \quad (5)$$

The lattice-spacing is fixed to 51 µm, *i.e.* three times the resolution of the µCT scans, to reduce the computational effort. The nodes of the lattice are located at the centre of (51 µm)$^3$ voxels. Since we simulated the fluid flow in a whole bioreactor chamber, the computational domain (see Supplementary material, Fig. S2) comprises about 270 x 270 x 540 nodes.

The time step $\Delta t$ is selected such as the compressibility effects in the LBM remain negligible. This constraint reads:

$$\frac{v_{max}}{(\Delta x/\Delta t)} \lesssim 0.1 c_s \quad (6)$$

where $v_{max}$ is the maximum velocity reached by the fluid in the domain.

A flat and constant velocity profile is set at the inlet of the chamber, *i.e.* the component of the fluid velocity parallel to bioreactor axis is equal to $v_s = 1.47$ mm.s$^{-1}$. $v_s$ is the superficial velocity, *i.e.* the ratio of the perfusion flow rate $Q$ to the tube cross-section. A zero velocity gradient is assumed at the outlet[49]. The complex solid boundaries (associated with the bioreactor walls and the spheres or cubes forming the granular packed bed) are approximated by a staircase shape (in accordance with the voxel representation provided by the µCT scans). A no-slip (zero velocity) condition is assumed on the solid surfaces. This assumption is relevant because the spheres and the cubes are non-porous. The no-slip condition is modelled by the so-called bounce-back rule, in which a fictitious particle incident on the boundary reverses its direction. In this way, the fictitious particles are kept out of the obstacles and the null velocity condition is satisfied at the solid surface. The solid surface is located halfway between the "fluid node" and the "solid node" forming the obstacle.

We ran LBM simulations until fluid flow reached steady state.

239

240 **Wall shear stress computation**

241 To determine the WSS that the fluid exerted, the viscous stress tensor $\bar{\bar{\sigma}}$ and the wall normal
242 vector $\vec{n}$ are required. The modulus of the wall shear stress $\tau$ is indeed given by:

243 $$\tau = \left|\bar{\bar{\sigma}} \cdot \vec{n} - \left((\bar{\bar{\sigma}} \cdot \vec{n}) \cdot \vec{n}\right) \vec{n}\right| \quad (7)$$

244 The viscous stress tensor can be calculated at each neighbour node of a solid surface from the
245 LBM velocity distribution function at that node. The nodes (and associated voxels)
246 neighbouring a solid surface (spheres, cubes or bioreactor lateral inner walls) are further
247 referred to as scaffold surface sites. The generic term $\sigma_{\alpha\beta}$ of the viscous stress tensor (in real
248 units) is given by:

249 $$\sigma_{\alpha\beta} = \left(\frac{\omega_1}{2} - 1\right)\left(\rho\left(\frac{\Delta x}{\Delta t}\right)^2 \left(\sum_{i=0}^{q} f_i c_{i\alpha} c_{i\beta}\right) - v_\alpha v_\beta - P\delta_{\alpha\beta}\right) \quad (8)$$

250 where $c_{i\alpha}$ is the $\alpha$-component ($\alpha = x, y$ or $z$) of the particle velocity $\vec{c}_i$, $v_\alpha$ is the $\alpha$-
251 component of the fluid velocity $\vec{v}$ and $\delta_{\alpha\beta}$ is the Kronecker symbol.

252 The determination of the boundary normal vector is not as straightforward, due to the
253 staircase shape of the solid boundary. We implemented a technique proposed by Stahl [50] to
254 detect locally the wall normal direction. This method relies on the fluid flow properties near
255 the solid boundary and not on the boundary geometry itself, as in the marching cubes
256 algorithm [51]. We refer the interested reader to the original article of Stahl et al. [50] if he wishes
257 further information.

258 We computed the probability density function (PDF) of the wall shear stress modulus as
259 follows: the wall shear stress range is divided into bins of equal size, *i.e.* $\Delta\tau = 1$ mPa. The

value of the PDF in the i-th bin is equal to $N(i)/\left(\Delta\tau \sum_j N(j)\right)$ where $N(i)$ is the number of scaffold surface sites with WSS falling into the interval $[(i-1)\Delta\tau\,;\, i\Delta\tau]$. We also defined a conditional PDF as the PDF of the WSS conditioned to the local presence of cells at a given cultivation time. The value of the conditional PDF in the i-th bin is equal to $N_c(i)/\left(\Delta\tau \sum_j N_c(j)\right)$ where $N_c(i)$ is the number of scaffold surface sites covered by cells at that time with WSS falling into the interval $[(i-1)\Delta\tau\,;\, i\Delta\tau]$.

**Statistical Analysis**

Experiments were carried out three times independently. Analyses were performed using GraphPad Prism software (GraphPad).

# Results

## Cell visualization by µCT

Osmium tetroxide allowed us to increase the density of the cell fraction and, in combination with biomaterials chosen for their low X-ray attenuation properties (polyacetal, d=1,41g/cm$^3$; PDMS, d=1,1g/cm$^3$), we were able to visualize cells with a high signal to background ratio (Fig. 1). We optimized this approach to facilitate the quantification procedure based on threshold method for converting the grey-scaled image into a binary one. Thus, it was possible for us to separate the scaffold from cells.

## Quantification, spatial distribution and dynamic of cell proliferation within the construct

We prepared the granular packed bed by stacking POM spheres or PDMS cubes. We then used this as a scaffold to investigate cell proliferation under a steady flow rate (10 mL/min). We investigated cell proliferation over 3 weeks by X-ray µCT visualization. During the experiment, we were able to visualize cell proliferation over the entire volume of the bioreactor (3 cm$^3$) (Fig. 2). Over the 3 weeks of culture, we quantified the total cellular volume and simultaneously evaluated the local cell proliferation with regards to scaffold geometry (Figure 2-B, 2-D). Quantification of the cellular volume revealed a considerable increase from 3.6 mm$^3$ ± 1.9 at week 1 to 60.7 mm$^3$ ± 24.4 at week 3 for spheres and an increase from 0.82 mm$^3$ ± 0.13 at week 1 to 15.75 mm$^3$ ± 1.20 at week 3 for cubes. Knowing the volume of the cell phase for each culture time and the average volume of a fibroblast NIH-3T3 ($\vartheta = 1540$ µm$^3$/fibroblast) [52], it is possible to estimate the cell number. To validate this hypothesis, additional experiments were carried out with spheres. After 1 week, the cell phase volume was 3.6±1.9 mm$^3$ which represents 2.2±1.0 million cells. Then, this data can be compared to the real number of cells obtained by cell count. These data are in good agreement

with the cell counts carried out after one week of bioreactor culture on independent samples (2.5 million cells).

Interestingly, for cubes, while homogeneous increase in area colonized by cells was observed during the first 2 weeks along the longitudinal axis of the bioreactor, local variations were noticed at week 3 (Fig. 3). These local variations were observed with a periodic recurrence of 3 mm, which corresponds to the size of the PDMS cube (Fig. 3-A), and maxima were located in between the horizontal cube/cubes contact zone. Local variations of the cellular volume were also observed for spheres (Fig. 3-B), although to a lesser extent, with a periodic recurrence of 2 mm, which corresponds to the diameter of the spheres.

Analysis of volume distribution within the bioreactors allowed us to distinguish 3 classes of cell aggregates, namely Small aggregates (with a volume below 1000 voxels; <2,500 fibroblasts), Medium aggregates (volume comprised between 1000 and 10,000 voxels; between 2,500 and 25,000 fibroblasts) and Large aggregates (volume superior to 10,000 voxels; > 25,000 fibroblasts). Such distinctions allowed us to describe the proliferative mechanism with regards to volume expansion observed within the constructs. We further analyzed the volume and the number of cell aggregates within the bioreactor to better understand the dynamics of cell proliferation over time-course of the experiment (Fig. 4). When cultured on PDMS cubes under steady flow rate, we noticed that after 1, 2 or 3 weeks of culture, Small aggregate were the most numerous within the bioreactor (Fig. 4-A). However, the cellular volume they represent was constantly decreasing over the time of culture. After 1 week of culture, they represented 55% of the cellular volume while decreasing to 23.2% after 2 weeks and represented only 7.6% at week 3. Interestingly, we observed the inverse phenomenon for large aggregates. At week 1 only 1 large aggregate was detected, representing itself 14.54% of the cellular biomass at this time point. At week 2, 23 Large aggregates were detected representing a volume of 29.8% of the total cellular volume

and finally, at week 3 Large aggregates (n=95) accounted for 67.3% of the cellular volume. This inverted correlation between Small and Large aggregates can be explained by the constant cellular proliferation within the bioreactor, therefore when growing, Small aggregates, finally become Large. This explanation is in agreement with the increase in Medium aggregates at weeks 2 that seems to be "fed" by the growing of Small aggregates. Themselves, Medium aggregates "feed" Large aggregates at week 3 by growth and coalescence. It is worth to note that the cellular distribution profile of cells cultured on spheres is not similar to the one of cells cultured on cubes but is shifted from one week (Fig. 4-B). Indeed, week 1 profile of cells cultured on spheres is similar to the week 2 profile of cells cultured on cubes. A similar observation can be made for week 2 profile of cells culture on spheres, which is similar to the week 3 profile of cells cultured on cubes.

**Fluid flow and mechanical stimulation**

Hydrodynamics within the bioreactors depend on the culture medium flow rate, on its viscosity, and on the construct geometry. From images captured by X-ray μCT, we obtained the scaffold geometry and the real distribution in time and space of the cells within the scanned volume. We focused on the constructs perfused during 3 weeks. Indeed, the comparative analysis between the wall shear stress distribution and the local presence of cells is statistically more robust when the scaffolds are more cellularized. We calculated fluid flow and wall shear stress on the scaffold surface at the beginning of cultivation (*i.e.* without the cellular phase) using an in-house lattice-Boltzmann code.

Fig. 5-A1, 5-B1 and Fig. 5-A2, 5-B2 show typical maps of the fluid velocity modulus as well as a map of the wall shear stress in the same horizontal plane. We note that the highest wall shear stress values arose around the pores where the fluid flows most quickly. We determined the probability density function (PDF) of the shear stress exerted by the fluid on the scaffold

surface at the beginning of cultivation. The PDF were computed with a bin size of 0.5 mPa. Fig. 5-A3 and Fig. 5-B3 show that the PDF of the wall shear stress is narrower for the stacking of cubes than for the stacking of spheres and the WSS is half as low on average. Indeed, for the stacking of spheres (resp. cubes), the wall shear stress within the bioreactor ranges between 0 and 130 mPa (resp. between 0 and 100 mPa). The first, the fifth and the ninth deciles are equal to 5 mPa, 18 mPa and 37 mPa (resp. to 2 mPa, 9 mPa and 21 mPa). The mean WSS is equal to 20 mPa (resp. 11 mPa) and the standard deviation of the PDF is equal to 13 mPa (resp. 8 mPa). We emphasize that the error bars (which presently represents one standard deviation bellow and above the mean value, calculated from three independent experiments) on the PDF are larger for the stackings of cubes. This is attributed to the greater variability of stacking.

To quantify the wall shear stress occurring in the regions that the cells preferentially cover, we computed the PDF of the wall shear stress at the beginning of cultivation conditioned to the local presence of cells after three weeks of cultivation (Fig. 5-A3 and 5-B3). It appears that the conditional PDF is slightly shifted toward higher shear stresses (WSS mean value increases by 4%) for spheres whereas it is slightly shifted toward lower WSS (WSS mean value decreases by 4%) for cubes. This effect is more significant at low WSS: the first decile is shifted from 5 mPa to 7 mPa for the spheres where as it is shifted from 2 mPa to 1 mPa for the cubes.

In order to link the values taken by the wall shear stress to the presence of cells (regardless of the frequency of the WSS values within the bioreactor), we calculated the ratio of the conditional PDF to the “standard” one. This ratio can be interpreted as the occupancy of the scaffold surface sites characterized by a given value of the wall shear stress, normalized by the construct surface coverage with cells. We defined the occupancy of a given class of scaffold sites as the fraction of sites (from this class) covered by cells after three weeks of

cultivation. The construct surface coverage is the fraction of scaffold surface covered by cells regardless of the wall shear stress value. Fig. 5-A4 and Fig. 5-B4 present the variations of the PDF ratio over the interval $[0\ \text{mPa}; 60\ \text{mPa}]$ for the stacking of spheres and the stacking of cubes, respectively. We chose 60 mPa as an upper bound since it coincides with the $99^{\text{th}}$ centile of the PDF for spheres (the $99^{\text{th}}$ centile of the PDF for cubes is lower, *i.e.* about 40 mPa). We adapted the bin size according to the intensity of the WSS to obtain more reliable values: since the probability to find large values of the WSS within the bioreactor is low (the PDF tends to zero as the WSS becomes high), the uncertainty on the PDF values is high in that range and the uncertainty on the PDF ratio even higher.

Fig. 5-A4 shows that for the stacking of spheres, the relative occupancy of the surface sites is minimal when WSS is zero. It increases with WSS over the interval $[0\ \text{mPa} ; 20\ \text{mPa}]$ and reaches a plateau above 20 mPa. The surface sites with WSS below 10 mPa are less covered by cells than average (PDF ratio lower than 1). The picture is different and less clear for the stacking of cubes (Fig. 5-B4). It seems more difficult to identify a definite trend. The relative occupancy of the surface sites appears maximal when WSS is close to zero. It decreases with WSS over the interval $[0\ \text{mPa}; 10\ \text{mPa}]$. The relative occupancy reaches a plateau between 10 mPa and about 20 mPa. Above 20 mPa, the relative occupancy appears erratic and scattered: a reasonable increase in bin size does not compensate for the decrease in the number of events per bin.

# Discussion

Methodology combining histological procedure and image analysis allows the description and quantification of cell proliferation within bioreactor[53]. However, this method can only generate a crude rather than comprehensive depiction of the 3D scaffold, primarily because its destructive nature leads to an incomplete representation of the 3D tissue. Over the last ten years, non-destructive three-dimensional image-based technology has made steady progress (*i.e.* the ability to visualize micrometric objects)[54]. The notion of virtual histology, which involves a combination of tomography imaging and image processing to analyse 3D tissue-engineered emerged over this period [28,29]. Among these technologies, high-resolution X-ray micro-tomography offers non-invasive 3D visualization of biological scaffolds[26,27]. To study the effect of WSS on cells, the ideal method is to collect relevant information at the single-cell scale from the macroscopic bioreactor scale. This is made possible by coupling µCT imaging and numerical simulation. Computational fluid dynamics approaches have shown promising results to estimate wall shear stress distribution in idealized geometries and numerically reconstructed scaffold geometry from X-ray tomography[33–35,55,56]. To date, this strategy has been implemented with considerable success on single scaffold with a single-cell resolution without contrast agent [28,29]. This approach enables the assessment of cell proliferation (and mineralization) within the volume of 3D scaffolds. However, this method is difficult to apply at the macroscopic bioreactor scale. Although it is now possible to image with µCT volumes of several cubic centimeters by helical acquisition with a resolution close to that of a single-cell, the time required for the acquisition (30 hours in our case), the volume of data generated (more than 100 Giga octets in our case), and the computing power needed to visualize the image does not allow for this method to be used routinely. Compromises are necessary in terms of resolution. That is why in this study, despite being aware that we are losing some amount information, we chose a voxel of of 17*17*17 $\mu m^3$ equal to at least the volume of a

413 couple of fibroblasts[52] resulting in an acquisition time of 1.5 hours for 15 Giga octets. Major
414 limitations of μCT are related to the mechanisms involved in image acquisition. Scanned
415 biological materials become visible based on their attenuation of the X-ray energy beam[57].
416 Moreover, to be able to visualize the cell phase, we demonstrated the feasibility of improving
417 cell contrast at the macroscopic bioreactor scale by using osmium tetroxide[58] on constructs.
418 Then, from the μCT acquisitions, an accurate three-dimensional virtual representation of
419 constructs can be generated. This approach enables the qualitative and semi-quantitative
420 assessment of cell proliferation within the volume of constructs and allows us to generate 3D
421 objects that are directly usable for CFD simulations.

422 The interactions between fluid flow and living media are complex, and far from being fully
423 understood. Cell and tissue metabolism are typically influenced by the transport phenomena
424 of nutrients and oxygen that the flow controls. They may also be directly affected by the
425 viscous shear stresses [59] that fluid flow produces.
426 We simplified the perfusion culture method that is described in David & al [2] (stack of
427 microporous scaffolds). Our decision to reduce the double porosity to a single one was
428 motivated by the fact that the impact of WSS on cells has already been described during cell
429 cultures for microporous scaffolds [29,30] but never in the macroscopic porosity within a packed
430 bed bioreactor.
431 We checked that in our experiments, the transport of glucose and oxygen are not limiting
432 phenomena. An estimate of the relative decrease in concentration in species $i$ between the
433 bioreactor inlet and outlet is given by:

434 $$\frac{\Delta C_i}{C_0^i} = \frac{N_{cells} V_m^i}{Q C_0^i} \quad (9)$$

435 where $N_{cells}$ is the number of cells within the bioreactor at the time considered, $V_m^i$ is the
436 uptake of species $i$ and $C_0^i$ is the concentration in species $i$ at the inlet. The glucose uptake rate

is equal to about $10^{-16}$ mol.cell$^{-1}$.s$^{-1}$ [60] the oxygen uptake rate to $6 \times 10^{-17}$ mol.cell$^{-1}$.s$^{-1}$ [61]. The glucose initial concentration of the culture medium is equal to $C_0^{gl} = 25$ mol.m$^{-3}$, the oxygen initial concentration to $C_0^{O2} = 0.21$ mol.m$^{-3}$. The maximum number of cells obtained after 3 weeks of cultivation (among the three experiments) was about 60 million. The relative decrease in glucose concentration between the bioreactor inlet and outlet is then negligible (about 0.1%) and the relative decrease in oxygen concentration is less than 10%.

Furthermore, the cells located in the depth of the tissue are well fed. Assuming one-dimensional steady diffusion, the relative decrease in species $i$ across the cell layer growing on the sphere/cube surface reads:

$$\frac{\Delta C_i}{C_0^i} = \left( \cosh\left( \sqrt{\frac{V_m^i}{\vartheta \mathcal{D}_i}} s \right) \right)^{-1} \qquad (10)$$

where $s$ is the cell layer thickness, $\vartheta$ the average volume of a fibroblast and $\mathcal{D}_i$ the diffusion coefficient of species $i$. We measured that the maximal cell layer thickness at week 3 is of the order of 100 µm. The diffusion coefficient of oxygen is equal to $\mathcal{D}_{O2} = 3 \times 10^{-9}$ m$^2$.s$^{-1}$ and the diffusion coefficient of glucose to $\mathcal{D}_{gl} = 6.7 \times 10^{-10}$ m$^2$.s$^{-1}$. The relative decrease in glucose concentration across the cell layer is then estimated at 35% and the relative decrease in oxygen concentration at 6%. The oxygen (resp. glucose) concentration within the cell layer remains greater than the Michaelis-Menten constant for oxygen, *i.e.* $K_M^{O2} = 6 \times 10^{-3}$ mol.m$^{-3}$ (resp. glucose, *i.e.* $K_M^{gl} = 9$ mol.m$^{-3}$).

It should be noted that the conclusion could be different if the material constituting the beads or the cubes was porous (like coral for example). In that case, the resistance to solute transfer in the micropores of the material should be taken into account.

Using a lattice-Boltzmann method, we were able to simulate the fluid flow within our bioreactors and retrieve the local values of WSS on the scaffold' surface at the beginning of cultivation. Two kinds of scaffold were examined, *i.e.* stacking of cubes of 3 mm edge and

stacking of spheres of 2 mm diameter. We found that the distributions strongly differ: the PDF is narrower for the stacking of cubes than for the stacking of spheres. Furthermore, the mean WSS is lower for cubes (11 mPa) than for spheres (20 mPa). It is worth noting that the porosity of the stackings were very close, *i.e.* 46% and 45.5%, respectively, and the specific wetted areas were also similar, *i.e.* 707 $m^{-1}$ and 840 $m^{-1}$, respectively. We deduce that the discrepancies in WSS distribution are presently mainly due to the shape of the particles forming the granular bed (*i.e.* the scaffold) and to their spatial arrangement. Besides, the geometry of the particles directly impacts the way they pile up (see Fig. 1).

The ultimate goal of this study is knowing and controlling the level of stimulation in advance at the interface between the fluid and the cells. During the cell culture, the average WSS depends on the superficial velocity and on the construct porosity within the bioreactor. It is possible that simulations we performed on empty scaffolds would be slightly different after the start of culture [30]. The porosity of the construct may also vary over time due to cell proliferation and matrix deposition. In certain experiments conducted on highly porous (80%) PLA-nonwoven-fiber-mesh scaffold, it has been demonstrated [30] that the levels of WSS increase as a function of culture time. However, the pore size within this scaffold (and more generally scaffolds used in bone tissue engineering), around 100-200μm, is very different from that within a stack of cubes/beads in the bioreactor (≈1mm). In both cases, the increase in biomass within pores leads to a decrease in porosity, but pore clogging and subsequent liquid flow redistribution within the bioreactor occur in different time scales. In the present study, because the volume fraction of cells (about 1%) after three weeks of perfusion remains small compared to the porosity of the spheres-based scaffold (about 45%), because the pores within the stacks are macroscopic, we expect that the PDF of the WSS within the construct during the time course of cultivation does not significantly differ from the PDF at the beginning of cultivation.

As described in the results section, we also computed the PDF of the wall shear stress at the beginning of cultivation conditioned to the local presence of cells after three weeks of cultivation. We noted that for the same kind of particles, the conditional PDF is similar to the "standard" PDF: the general shape of the conditional PDF is more influenced by the WSS distribution within the bioreactor than by the presence of cells. In order to isolate the relation between the value of the wall shear stress and the presence of cells (regardless of the frequency of that WSS value within the bioreactor), we calculated the ratio of the conditional PDF to the "standard" one. This ratio represent the occupancy of the scaffold surface sites characterized by a given value of the wall shear stress, normalized by the construct surface coverage with cells.

We first note that, whatever the particle shape, *i.e.* cube or sphere, the relative occupancy of the surface sites by cells remains high (greater than 0.6) in the WSS range (from 0 mPa up to 60 mPa) presently investigated. We deduce that this WSS interval is generally favourable to cell proliferation. This finding is in line with the results reported by the literature for osteocompetent cells. *In vitro*, shear stresses ranging from 1 to 10 mPa enhance the cell proliferation [23], from 1 mPa to 50 mPa improve proliferation, matrix production, and mineralization [1,12,62,63] and values greater than 600 mPa [10,12,22,64,65] are detrimental for cell viability and adhesion. However, we hypothesize that with osteoblast cells, a longer culture time would be necessary to obtain the same cell expansion within the bioreactor than what is observed with fibroblasts after three weeks (osteoblasts doubling time is twice that of fibroblasts, about 48 hours against 24). In addition, the choice of fibroblasts rather than osteoblasts may be justified by the fact that our objective was to statistically correlate proliferation with shear levels. With osteoblasts, would have observed both proliferation and differentiation, thereby undermining our analysis.

As reported in the results section, we may distinguish different WSS intervals according to the relative occupancy of the scaffold surface sites by cells. These intervals depend on the shape of the particles constituting the granular bed. For the stacking of spheres, the relative occupancy of the surface sites by cells is maximal when WSS is greater than 20 mPa. For the stackings of cubes, the relative occupancy is maximal when the WSS is lower than 10 mPa. In the meantime, the quantification of cell proliferation reveals that the cellular volume at week 3 is four times higher in the stacking of spheres than in the stacking of cubes (*i.e*. about 61 $mm^3$ against 16 $mm^3$). We expect that the cell proliferation starts from the regions where the wall shear stress is low since cells are initially single (or possibly grouped together into small monolayered patches) at the scaffold surface and proliferation in that configuration requires wall shear stress as low as 5 mPa [12]. The maximal occupancy at zero WSS observed for the stacking of cubes is a direct consequence of that proliferation phase. When the cells form a multi-layered tissue-like structure, higher values of the WSS (up to 50 mPa) become also conducive to cell proliferation (and possibly even more conducive than lower values of WSS). This is precisely what we observe for the stackings of spheres. The formation of multi-layered structure require 3-D environments (at the cell scale). Such sites actually exist in stackings of beads: they are typically located at the contact point between beads [53]. On the contrary, stackings of cubes seem to have fewer sites able to induce 3-D (multi-layered) proliferation.

# Conclusion

Using a lattice-Boltzmann method, we computed the flow within the bioreactor and retrieved the local WSS potentially experienced by the cells during the cultivation time course. At a steady perfusion flow rate, the range of WSS occurring within the construct and influencing cell proliferation strongly depends on the geometry of the granular materials constituting the 3D based construct. Depending on the geometry of the scaffold considered, it seems that a given level of shear stress may be more or less beneficial in terms of cell proliferation, this benefit is not universal but seems geometry dependent.

This work presents a step toward a better mastering of tissue growth in a perfusion bioreactor. By knowing a priori the optimum level of mechanical stimulation required for cell expansion enhancement, the bioreactor perfusion flow rate can be adjusted in accordance with the optimal range presented in this study to obtain, on average, the desired stress value, within the construct. Also, we anticipate that our results, by reverse engineering, will help to design a bioreactor or scaffolds so that the majority of the shear stress values that the cells will experience during an perfusion culture are included in the ranges described in the present paper as beneficial for cell proliferation.

# Acknowledgments

The authors gratefully acknowledge the LabeX LaSIPS (ANR-10-LABX-0040-LaSIPS), managed by the French National Research Agency under the "Investissements d'avenir" programs, (n°ANR-11-IDEX-0003-02 and ANR-10-EQPX-37 MATMECA Grant) for their financial support.

## Author Disclosure Statement

The authors have no conflict of interest to declare, including competing financial interests. All of the co-authors confirm their agreement with this statement. All authors have been appropriately disclosed according to the policy of the Journal.

# References


1. Bancroft GN, Sikavitsas VI, van den Dolder J, Sheffield TL, Ambrose CG, Jansen JA, Mikos AG. Fluid flow increases mineralized matrix deposition in 3D perfusion culture of marrow stromal osteoblasts in a dose-dependent manner. *Proc Natl Acad Sci U S A*. 2002;99(20):12600-12605. doi:10.1073/pnas.202296599.

2. David B, Bonnefont-Rousselot D, Oudina K, Degat M-C, Deschepper M, Viateau V, Bensidhoum M, Oddou C, Petite H. A perfusion bioreactor for engineering bone constructs: an in vitro and in vivo study. *Tissue Eng Part C Methods*. 2011;17(5):505-516. doi:10.1089/ten.TEC.2010.0468.

3. Frohlich M, Grayson WL, Wan LQ, Marolt D, Drobnic M, Vunjak-Novakovic G. Tissue engineered bone grafts: biological requirements, tissue culture and clinical relevance. *Curr Stem Cell Res Ther*. 2008;3(4):254–264.

4. Grayson WL, Bhumiratana S, Cannizzaro C, Chao P-HG, Lennon DP, Caplan AI, Vunjak-Novakovic G. Effects of initial seeding density and fluid perfusion rate on formation of tissue-engineered bone. *Tissue Eng Part A*. 2008;14(11):1809-1820. doi:10.1089/ten.tea.2007.0255.

5. Griffin DJ, Vicari J, Buckley MR, Silverberg JL, Cohen I, Bonassar LJ. Effects of enzymatic treatments on the depth-dependent viscoelastic shear properties of articular cartilage. *J Orthop Res*. 2014;32(12):1652-1657. doi:10.1002/jor.22713.

6. McCoy RJ, O'Brien FJ. Influence of shear stress in perfusion bioreactor cultures for the development of three-dimensional bone tissue constructs: a review. *Tissue Eng Part B Rev*. 2010;16(6):587-601. doi:10.1089/ten.TEB.2010.0370.

7. Raimondi MT, Moretti M, Cioffi M, Giordano C, Boschetti F, Laganà K, Pietrabissa R. The effect of hydrodynamic shear on 3D engineered chondrocyte systems subject to direct perfusion. *Biorheology*. 2006;43(3-4):215-222.

8. Goldstein AS, Juarez TM, Helmke CD, Gustin MC, Mikos AG. Effect of convection on osteoblastic cell growth and function in biodegradable polymer foam scaffolds. *Biomaterials*. 2001;22(11):1279-1288.

9. Grayson WL, Marolt D, Bhumiratana S, Fröhlich M, Guo E, Vunjak-Novakovic G. Optimizing the medium perfusion rate in bone tissue engineering bioreactors. *Biotechnol Bioeng*. 2011;108(5). doi:10.1002/bit.23024.

10. Hung CT, Pollack SR, Reilly TM, Brighton CT. Real-time calcium response of cultured bone cells to fluid flow. *Clin Orthop*. 1995;(313):256-269.

11. Jungreuthmayer C, Jaasma MJ, Al-Munajjed AA, Zanghellini J, Kelly DJ, O'Brien FJ.

590 Deformation simulation of cells seeded on a collagen-GAG scaffold in a flow perfusion
591 bioreactor using a sequential 3D CFD-elastostatics model. *Med Eng Phys*. 2009;31(4):420-
592 427. doi:10.1016/j.medengphy.2008.11.003.

593 12. Leclerc E, David B, Griscom L, Lepioufle B, Fujii T, Layrolle P, Legallaisa C. Study of
594 osteoblastic cells in a microfluidic environment. *Biomaterials*. 2006;27(4):586-595.
595 doi:10.1016/j.biomaterials.2005.06.002.

596 13. Park JY, Yoo SJ, Patel L, Lee SH, Lee S-H. Cell morphological response to low shear
597 stress in a two-dimensional culture microsystem with magnitudes comparable to interstitial
598 shear stress. *Biorheology*. 2010;47(3-4):165-178. doi:10.3233/BIR-2010-0567.

599 14. Pedersen JA, Boschetti F, Swartz MA. Effects of extracellular fiber architecture on cell
600 membrane shear stress in a 3D fibrous matrix. *J Biomech*. 2007;40(7):1484-1492.
601 doi:10.1016/j.jbiomech.2006.06.023.

602 15. Sikavitsas VI, Bancroft GN, Holtorf HL, Jansen JA, Mikos AG. Mineralized matrix
603 deposition by marrow stromal osteoblasts in 3D perfusion culture increases with increasing
604 fluid shear forces. *Proc Natl Acad Sci U S A*. 2003;100(25):14683-14688.
605 doi:10.1073/pnas.2434367100.

606 16. Horikawa A, Okada K, Sato K, Sato M. Morphological changes in osteoblastic cells
607 (MC3T3-E1) due to fluid shear stress: cellular damage by prolonged application of fluid shear
608 stress. *Tohoku J Exp Med*. 2000;191(3):127-137.

609 17. McGarry JG, Klein-Nulend J, Mullender MG, Prendergast PJ. A comparison of strain
610 and fluid shear stress in stimulating bone cell responses--a computational and experimental
611 study. *FASEB J Off Publ Fed Am Soc Exp Biol*. 2005;19(3):482-484. doi:10.1096/fj.04-2210fje.

612 18. Jacobs CR, Temiyasathit S, Castillo AB. Osteocyte mechanobiology and pericellular
613 mechanics. *Annu Rev Biomed Eng*. 2010;12:369-400. doi:10.1146/annurev-bioeng-070909-
614 105302.

615 19. Delaine-Smith RM, Sittichokechaiwut A, Reilly GC. Primary cilia respond to fluid shear
616 stress and mediate flow-induced calcium deposition in osteoblasts. *FASEB J*. 2014;28(1):430–
617 439.

618 20. Hoey DA, Downs ME, Jacobs CR. The mechanics of the primary cilium: an intricate
619 structure with complex function. *J Biomech*. 2012;45(1):17-26.
620 doi:10.1016/j.jbiomech.2011.08.008.

621 21. Meyer U, Wiesmann HP, Kruse-Lösler B, Handschel J, Stratmann U, Joos U. Strain-
622 Related Bone Remodeling in Distraction Osteogenesis of the Mandible. *Plast Reconstr Surg*.
623 1999;103(3):800.
624 http://journals.lww.com/plasreconsurg/Abstract/1999/03000/Strain_Related_Bone_Remod

eling_in_Distraction.5.aspx. Accessed October 23, 2017.

22. Cartmell SH, Porter BD, García AJ, Guldberg RE. Effects of medium perfusion rate on cell-seeded three-dimensional bone constructs in vitro. *Tissue Eng*. 2003;9(6):1197-1203. doi:10.1089/10763270360728107.

23. Glowacki J, Mizuno S, Greenberger JS. Perfusion enhances functions of bone marrow stromal cells in three-dimensional culture. *Cell Transplant*. 1998;7(3):319-326.

24. Grayson WL, Bhumiratana S, Grace Chao PH, Hung CT, Vunjak-Novakovic G. Spatial regulation of human mesenchymal stem cell differentiation in engineered osteochondral constructs: effects of pre-differentiation, soluble factors and medium perfusion. *Osteoarthritis Cartilage*. 2010;18(5):714-723. doi:10.1016/j.joca.2010.01.008.

25. Janssen FW, Hofland I, Van Oorschot A, Oostra J, Peters H, Van Blitterswijk CA. Online measurement of oxygen consumption by goat bone marrow stromal cells in a combined cell-seeding and proliferation perfusion bioreactor. *J Biomed Mater Res A*. 2006;79(2):338–348.

26. Cancedda R, Cedola A, Giuliani A, Komlev V, Lagomarsino S, Mastrogiacomo M, Peyrin F, Rustichelli F. Bulk and interface investigations of scaffolds and tissue-engineered bones by X-ray microtomography and X-ray microdiffraction. *Biomaterials*. 2007;28(15):2505-2524. doi:10.1016/j.biomaterials.2007.01.022.

27. Cartmell S, Huynh K, Lin A, Nagaraja S, Guldberg R. Quantitative microcomputed tomography analysis of mineralization within three-dimensional scaffolds in vitro. *J Biomed Mater Res A*. 2004;69A(1):97-104. doi:10.1002/jbm.a.20118.

28. Voronov RS, VanGordon SB, Shambaugh RL, Papavassiliou DV, Sikavitsas VI. 3D Tissue-Engineered Construct Analysis via Conventional High-Resolution Microcomputed Tomography Without X-Ray Contrast. *Tissue Eng Part C Methods*. 2012;19(5):327-335. doi:10.1089/ten.tec.2011.0612.

29. Alam TA, Pham QL, Sikavitsas VI, Papavassiliou DV, Shambaugh RL, Voronov RS. Image-based modeling: A novel tool for realistic simulations of artificial bone cultures. *Technology*. 2016;4(04):229–233.

30. Williams C, Kadri OE, Voronov RS, Sikavitsas VI. Time-Dependent Shear Stress Distributions during Extended Flow Perfusion Culture of Bone Tissue Engineered Constructs. *Fluids*. 2018;3(2):25.

31. Holt GE, Halpern JL, Lynch CC, Devin CJ, Schwartz HS. Imaging analysis of the in vivo bioreactor: a preliminary study. *Clin Orthop*. 2008;466(8):1890.

32. Cruel M, Bensidhoum M, Nouguier-Lehon C, Dessombz O, Becquart P, Petite H, Hoc T. Numerical Study of Granular Scaffold Efficiency to Convert Fluid Flow into Mechanical Stimulation in Bone Tissue Engineering. *Tissue Eng Part C Methods*. 2015;21(9):863-871.

660 doi:10.1089/ten.TEC.2014.0648.

661 33. Wittkowske C, Reilly GC, Lacroix D, Perrault CM. In vitro bone cell models: impact of
662 fluid shear stress on bone formation. *Front Bioeng Biotechnol*. 2016;4:87.

663 34. Zhao F, Mc Garrigle MJ, Vaughan TJ, McNamara LM. In silico study of bone tissue
664 regeneration in an idealised porous hydrogel scaffold using a mechano-regulation algorithm.
665 *Biomech Model Mechanobiol*. 2018;17(1):5–18.

666 35. Zhao F, Vaughan TJ, McNamara LM. Quantification of fluid shear stress in bone tissue
667 engineering scaffolds with spherical and cubical pore architectures. *Biomech Model*
668 *Mechanobiol*. 2016;15(3):561–577.

669 36. Korin N, Bransky A, Dinnar U, Levenberg S. A parametric study of human fibroblasts
670 culture in a microchannel bioreactor. *Lab Chip*. 2007;7(5):611-617. doi:10.1039/B702392H.

671 37. Penick KJ, Solchaga LA, Berilla JA, Welter JF. Performance of polyoxymethylene plastic
672 (POM) as a component of a tissue engineering bioreactor. *J Biomed Mater Res Part Off J Soc*
673 *Biomater Jpn Soc Biomater Aust Soc Biomater Korean Soc Biomater*. 2005;75(1):168–174.

674 38. Stražar K, Cör A, Antolic V. Biological impact of polyacetal particles on loosening of
675 isoelastic stems. *Biomacromolecules*. 2006;7(9):2507–2511.

676 39. Thompson MS, Northmore-Ball MD, Tanner KE. Tensile mechanical properties of
677 polyacetal after one and six months' immersion in Ringer's solution. *J Mater Sci Mater Med*.
678 2001;12(10-12):883–887.

679 40. Lee KI, Choi MJ. Phase velocity and normalized broadband ultrasonic attenuation in
680 polyacetal cuboid bone-mimicking phantoms. *J Acoust Soc Am*. 2007;121(6):EL263–EL269.

681 41. Braet F, De Zanger R, Wisse E. Drying cells for SEM, AFM and TEM by
682 hexamethyldisilazane: a study on hepatic endothelial cells. *J Microsc*. 1997;186(1):84–87.

683 42. Lee JTY, Chow KL. SEM sample preparation for cells on 3D scaffolds by freeze-drying
684 and HMDS. *Scanning*. 2012;34(1):12–25.

685 43. Porter B, Zauel R, Stockman H, Guldberg R, Fyhrie D. 3-D computational modeling of
686 media flow through scaffolds in a perfusion bioreactor. *J Biomech*. 2005;38(3):543-549.
687 doi:10.1016/j.jbiomech.2004.04.011.

688 44. Agitation induced cell injury in microcarrier cultures. Protective effect of viscosity is
689 agitation intensity dependent: Experiments and modeling - Lakhotia - 1992 - Biotechnology
690 and Bioengineering - Wiley Online Library.
691 http://onlinelibrary.wiley.com/doi/10.1002/bit.260390114/abstract. Accessed October 23,
692 2017.

693 45. Bağcı Ö, Dukhan N, Özdemir M. Flow regimes in packed beds of spheres from pre-
694 Darcy to turbulent. *Transp Porous Media*. 2014;104(3):501–520.

695 46. d'Humières D. Multiple–relaxation–time lattice Boltzmann models in three
696 dimensions. *Philos Trans R Soc Lond Math Phys Eng Sci*. 2002;360(1792):437–451.

697 47. Ginzburg I. Lattice Boltzmann modeling with discontinuous collision components:
698 Hydrodynamic and advection-diffusion equations. *J Stat Phys*. 2007;126(1):157–206.

699 48. Ginzburg I, d'Humières D. Multireflection boundary conditions for lattice Boltzmann
700 models. *Phys Rev E*. 2003;68(6):066614. doi:10.1103/PhysRevE.68.066614.

701 49. Duval H, Masson D, Guillot J-B, Schmitz P, d'Humières D. Two-dimensional lattice–
702 Boltzmann model of hydrosol depth filtration. *AIChE J*. 2006;52(1):39-48.
703 doi:10.1002/aic.10606.

704 50. Stahl B, Chopard B, Latt J. Measurements of wall shear stress with the lattice
705 Boltzmann method and staircase approximation of boundaries. *Comput Amp Fluids*.
706 39(9):1625-1633.
707 http://www.academia.edu/15314228/Measurements_of_wall_shear_stress_with_the_lattic
708 e_Boltzmann_method_and_staircase_approximation_of_boundaries. Accessed October 23,
709 2017.

710 51. Cline HE, Lorensen WE. System and method for the display of surface structures
711 contained within the interior region of a solid body. December 1987.

712 52. Echave P, Conlon IJ, Lloyd AC. Cell size regulation in mammalian cells. *Cell Cycle
713 Georget Tex*. 2007;6(2):218-224. doi:10.4161/cc.6.2.3744.

714 53. Chabanon M, Duval H, Grenier J, Beauchesne C, Goyeau B, David B. Histological
715 Method to Study the Effect of Shear Stress on Cell Proliferation and Tissue Morphology in a
716 Bioreactor. *Tissue Eng Regen Med*. March 2019. doi:10.1007/s13770-019-00181-3.

717 54. Farahani N, Braun A, Jutt D, Huffman T, Reder N, Liu Z, Yagi Y, Pantanowitz L. Three-
718 dimensional Imaging and Scanning: Current and Future Applications for Pathology. *J Pathol
719 Inform*. 2017;8. doi:10.4103/jpi.jpi_32_17.

720 55. Porter BD, Lin ASP, Peister A, Hutmacher D, Guldberg RE. Noninvasive image analysis
721 of 3D construct mineralization in a perfusion bioreactor. *Biomaterials*. 2007;28(15):2525-
722 2533. doi:10.1016/j.biomaterials.2007.01.013.

723 56. Voronov R, VanGordon S, Sikavitsas VI, Papavassiliou DV. Computational modeling of
724 flow-induced shear stresses within 3D salt-leached porous scaffolds imaged via micro-CT. *J
725 Biomech*. 2010;43(7):1279–1286.

726 57. de Bournonville S, Vangrunderbeeck S, Kerckhofs G. Contrast-Enhanced MicroCT for

727 Virtual 3D Anatomical Pathology of Biological Tissues: A Literature Review. *Contrast Media*
728 *Mol Imaging*. 2019;2019. doi:10.1155/2019/8617406.

729 58. Scheller EL, Troiano N, VanHoutan JN, Bouxsein MA, Fretz JA, Xi Y, Nelson T, Katz G,
730 Berry R, Church CD, Doucette CR, Rodeheffer MS, MacDougald OA, Rosen CJ, Horowitz MC.
731 Use of Osmium Tetroxide Staining with Microcomputerized Tomography to Visualize and
732 Quantify Bone Marrow Adipose Tissue In Vivo. *Methods Enzymol*. 2014;537:123-139.
733 doi:10.1016/B978-0-12-411619-1.00007-0.

734 59. Chen CS. Mechanotransduction–a field pulling together? *J Cell Sci*.
735 2008;121(20):3285–3292.

736 60. Cremer T, Werdan K, Stevenson AFG, Lehner K, Messerschmidt O. Aging in vitro and
737 D-glucose uptake kinetics of diploid human fibroblasts. *J Cell Physiol*. 1981;106(1):99–108.

738 61. Cho CH, Park J, Nagrath D, Tilles AW, Berthiaume F, Toner M, Yarmush ML. Oxygen
739 uptake rates and liver-specific functions of hepatocyte and 3T3 fibroblast co-cultures.
740 *Biotechnol Bioeng*. 2007;97(1):188–199.

741 62. Liegibel UM, Sommer U, Bundschuh B, Schweizer B, Hilscher U, Lieder A, Nawroth P,
742 Kasperk C. Fluid shear of low magnitude increases growth and expression of TGFbeta1 and
743 adhesion molecules in human bone cells in vitro. *Exp Clin Endocrinol Diabetes Off J Ger Soc*
744 *Endocrinol Ger Diabetes Assoc*. 2004;112(7):356-363. doi:10.1055/s-2004-821014.

745 63. Hillsley MV, Frangos JA. Alkaline phosphatase in osteoblasts is down-regulated by
746 pulsatile fluid flow. *Calcif Tissue Int*. 1997;60(1):48-53.

747 64. Weinbaum S, Cowin SC, Zeng Y. A model for the excitation of osteocytes by
748 mechanical loading-induced bone fluid shear stresses. *J Biomech*. 1994;27(3):339–360.

749 65. Mygind T, Stiehler M, Baatrup A, Li H, Zou X, Flyvbjerg A, Kassem M, Bünger C.
750 Mesenchymal stem cell ingrowth and differentiation on coralline hydroxyapatite scaffolds.
751 *Biomaterials*. 2007;28(6):1036-1047. doi:10.1016/j.biomaterials.2006.10.003.

752

753

## Figures legends

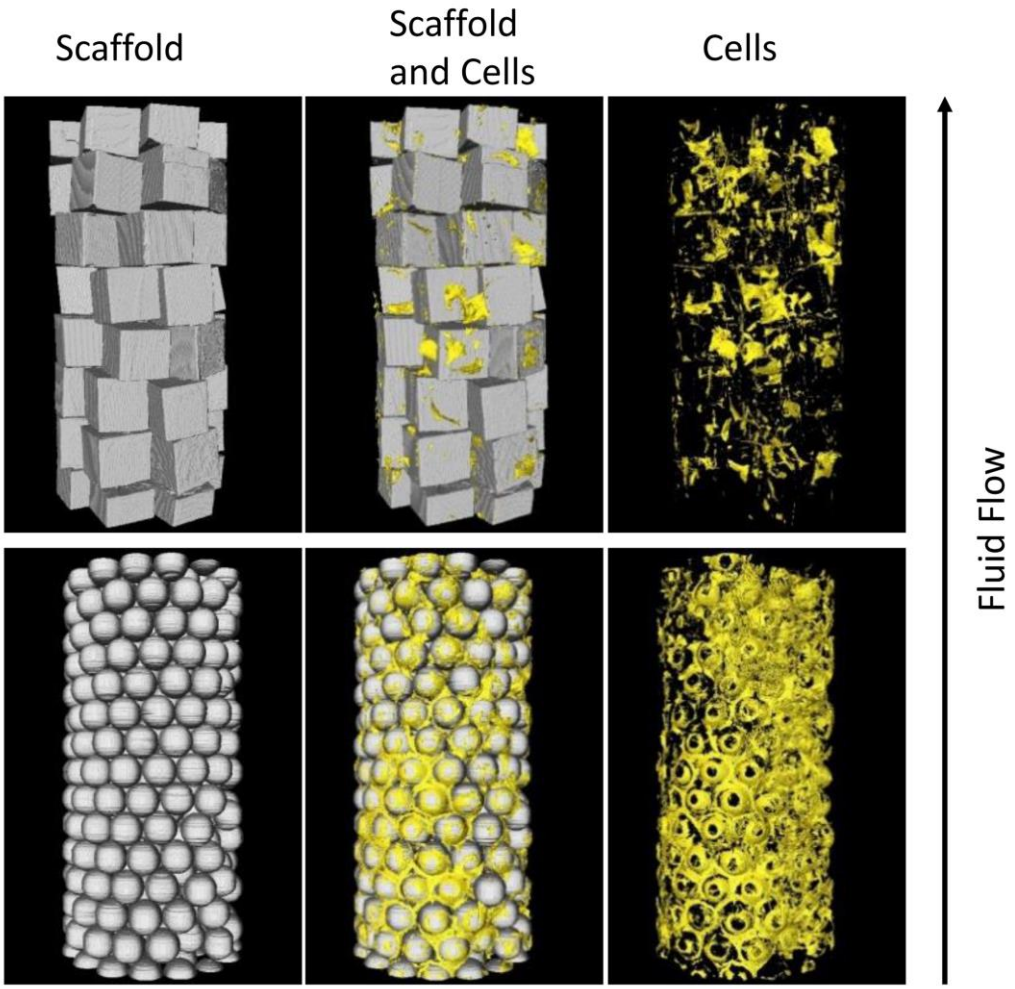


**Figure 1: Cell visualization by X-ray micro Ct within perfusion bioreactors**

3D-reconstruction of X-ray µCT acquisitions of cell culture in bioreactor enables the differentiation of scaffold from cells. PDMS cubic scaffold and POM spheres were seeded with fibroblasts and cultured under an upward flow of 10 mL/min for 3 weeks. Cells were fixed in 4% paraformaldehyde + 0.5 % glutaraldehyde, stained with osmium tetroxide and visualized by X-ray µCT. Based on image contrast enhanced by $OsO_4$ staining, image processing prior to 3D-reconstruction uses threshold methods to convert grey-scaled images into a binary ones. Staining and image binarization allow the mapping of native cellular organization.

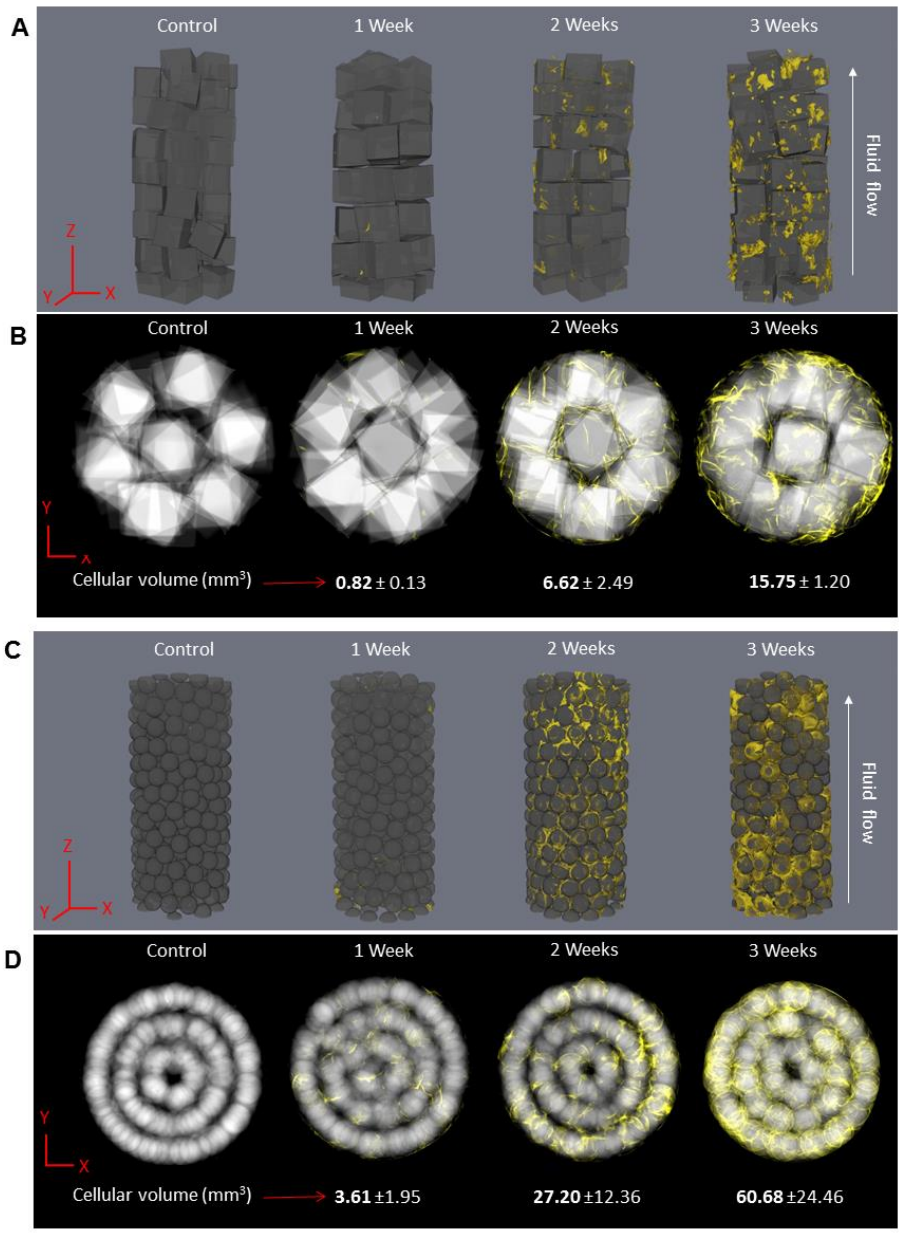


765

766 **Figure 2: Cells grow homogeneously over time within perfusion bioreactors**

767 3D-reconstructions and Z projections of X-ray µCT acquisitions of bioreactor cell cultures
768 over time show a homogeneous cell proliferation. Spheres and cubes-based bioreactors were
769 seeded with fibroblasts and fixed after 1, 2 or 3 weeks of culture under perfusion flow. Non-
770 seeded scaffold is shown as control. Both 3D reconstructions and Z projections illustrate the
771 homogeneous cell growth within the whole volume of the bioreactor regardless the
772 architecture of the scaffold. The total cellular volume was measured based on 3D-
773 reconstructions for the 3 time points.

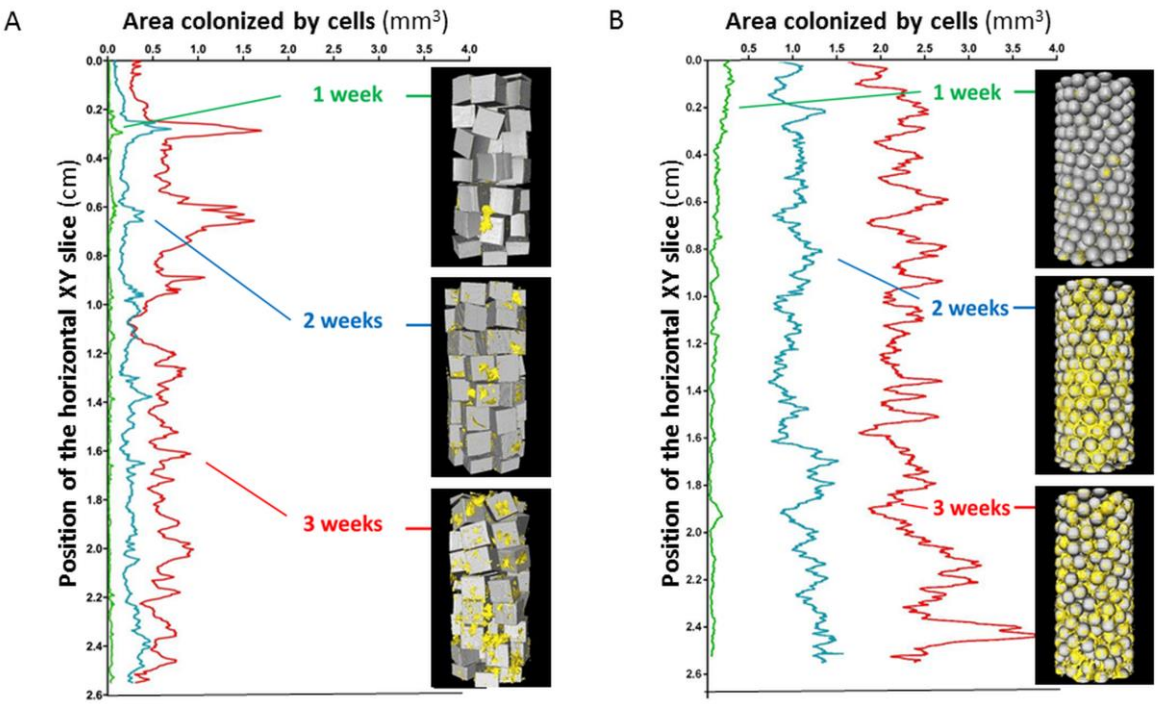


774

775 **Figure 3: Quantification of cell proliferation, distribution and organization within**

776 **perfusion bioreactors over time**

777 Local cell proliferation was measured for each XY section: surface area covered by cells is

778 plotted as a function of its position along the Z-axis (flow direction), for the 3 time points

779 (green: week 1, blue: week 2, red: week 3).

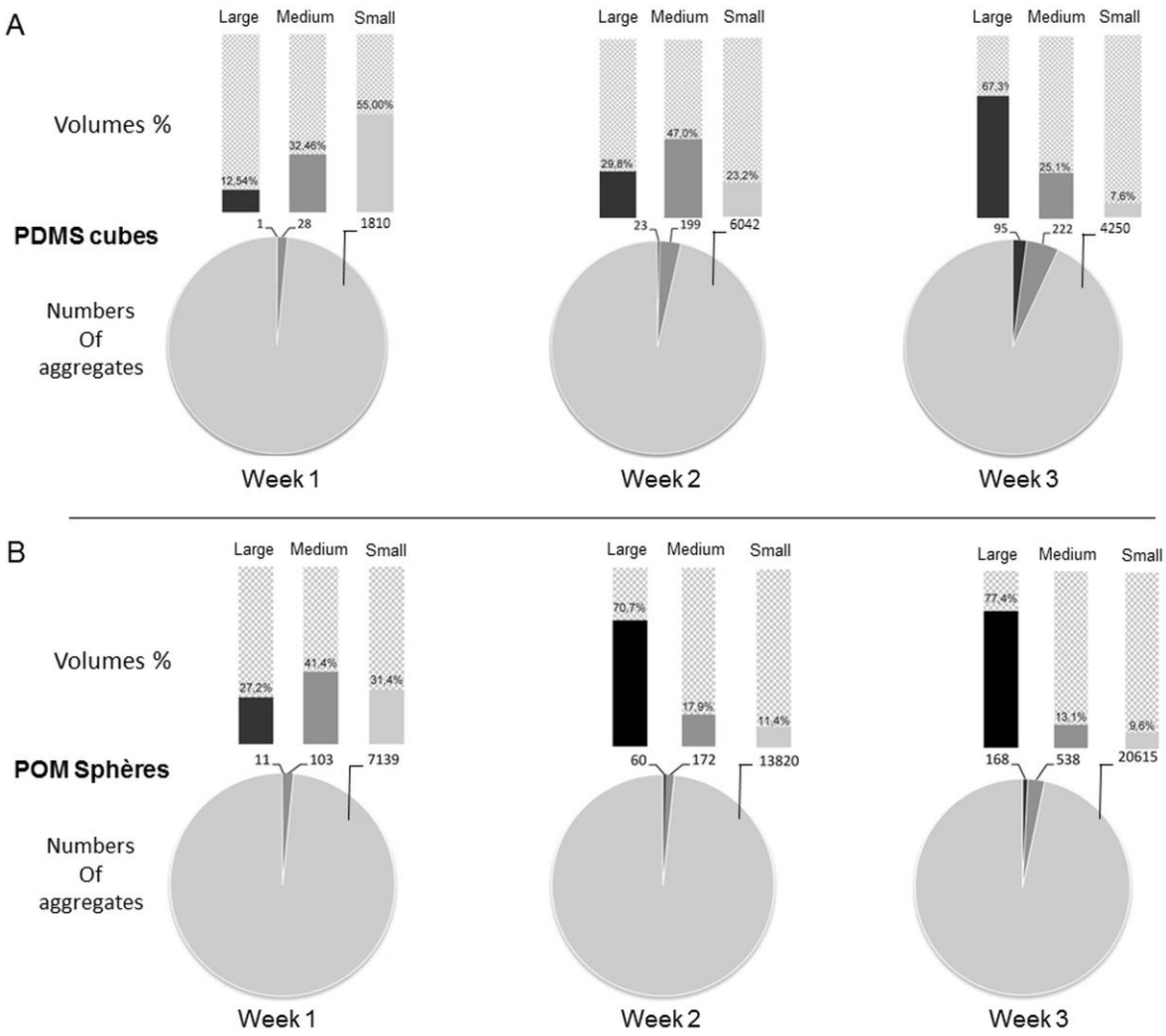


**Figure 4: Constant cellular proliferation feeds the pool of large cellular aggregates**

Using 3D-reconstructions for the 3 time points, number of cellular aggregates and the respective volume they occupy within the cellular phase were measured for spheres-based (A) and cubes-based (B) constructs. For both scaffolds, large cellular aggregates remain the less numerous though they rapidly represent the more volumic category of cellular aggregates.

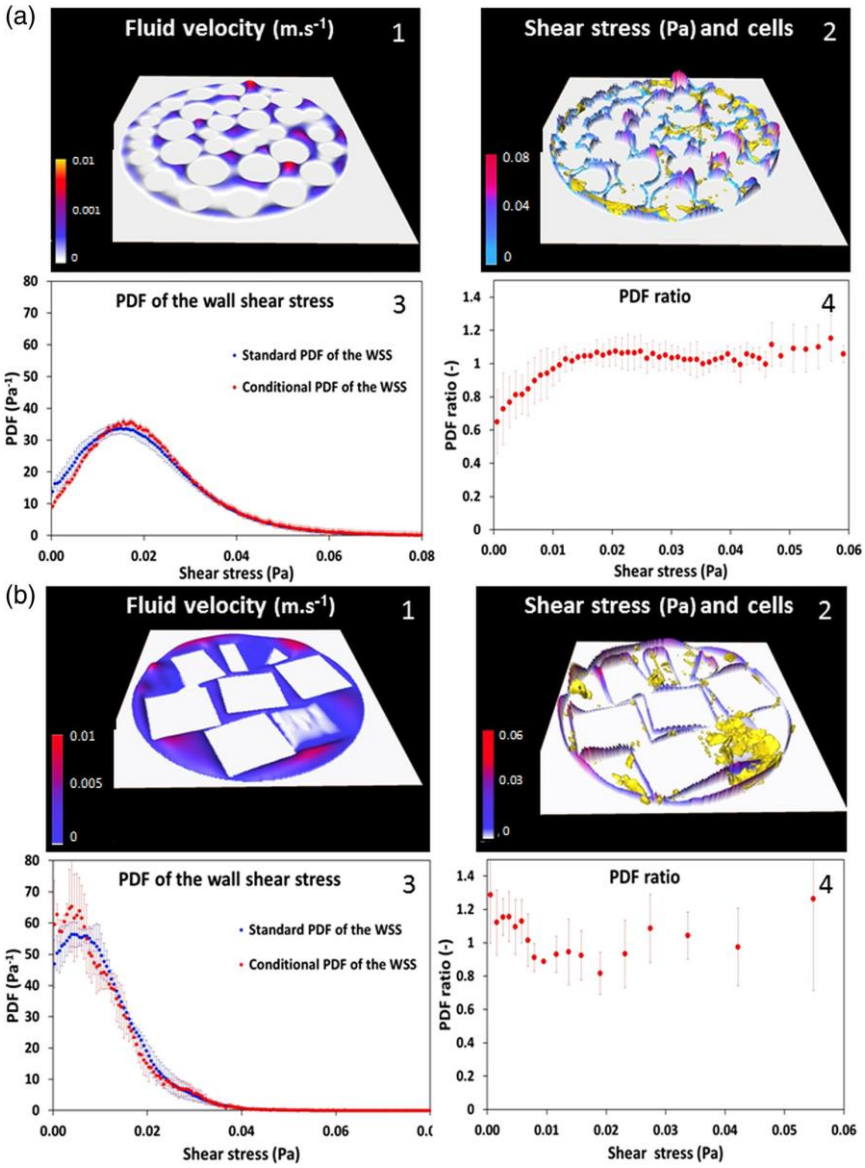


**Figure 5: 3-D lattice-Boltzmann simulations enables fine description of the optimal shear stress for cell proliferation.**

Map of the fluid velocity modulus (A1-B1), map of the wall shear stress and spatial distribution of cells (A2-B2) in the same horizontal plane. Standard wall shear stress Probability Density Function (PDF) and conditional PDF (*i.e.* the PDF of the wall shear stress conditioned to the local presence of cells after three weeks of perfusion) are simultaneously plotted as a function of wall shear stress (A3-B3). The PDF ratio (which represents the occupancy of the sphere surface sites characterized by a given value of the wall shear stress) is plotted as a function of the wall shear stress (A4-B4).

**Figure S1: Particle velocity vectors associated with the $d3q19$ lattice-Boltzmann method**

Voxel (black solid line), lattice node (in green) and particle velocity vectors (in red).

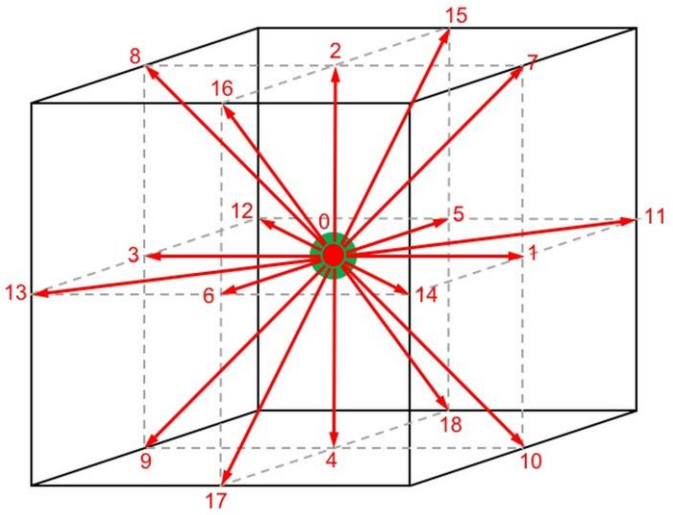

**Figure S2: Schematic of the computational domain**

The walls of the bioreactor are displayed in grey and the scaffold in brown. "Fluid" nodes are represented by small hollow circles, "solid" nodes by black filled circles and the links between nodes by black solid lines. Yellow zones correspond to the inlet and to the outlet. At the inlet, the particle populations entering the domain (associated with the red vectors) are adjusted with respect to the particle populations leaving the domain (blue vectors) in order to achieved the set fluid velocity profile (purple arrows). At the outlet, the particle populations entering the domain are equal to the corresponding populations at the penultimate nodes (with respect to the direction of the flow) in order to achieve the zero velocity gradient condition [49]. When a particle population encounters an obstacle, it reverses its direction (bounce-back rule).